ACS APPLIED MATERIALS & INTERFACES

Research Article

www.acsami.org

Fabrication of Multiple Heterojunctions with Tunable Visible-Light-Active Photocatalytic Reactivity in BiOBr–BiOI Full-Range Composites Based on Microstructure Modulation and Band Structures

Hongwei Huang,*[,†] Xu Han,[†] Xiaowei Li,[†] Shichao Wang,[‡] Paul K. Chu,[§] and Yihe Zhang*[,†]

[†]Beijing Key Laboratory of Materials Utilization of Nonmetallic Minerals and Solid Wastes, National Laboratory of Mineral Materials, School of Materials Science and Technology, China University of Geosciences, Beijing 100083, China

[‡]Department of Chemistry, Northwestern University, Evanston, Illinois 60208, United States

[§]Department of Physics and Materials Science, City University of Hong Kong, Tat Chee Avenue, Kowloon, Hong Kong China

Supporting Information

ABSTRACT: The fabrication of multiple heterojunctions with tunable photocatalytic reactivity in full-range BiOBr–BiOI composites based on microstructure modulation and band structures is demonstrated. The multiple heterojunctions are constructed by precipitation at room temperature and characterized systematically. Photocatalytic experiments indicate that there are two types of heterostructures with distinct photocatalytic mechanisms, both of which can greatly enhance the visible-light photocatalytic performance for the decomposition of organic pollutants and generation of photocurrent. The large separation and inhibited recombination of electron–hole pairs rendered by the heterostructures are confirmed by electrochemical impedance spectra (EIS) and photoluminescence (PL). Reactive species trapping, nitroblue tetrazolium (NBT, detection agent of $^{\bullet}O_2^-$) transformation, and terephthalic acid photoluminescence (TA-PL) experiments verify the charge-transfer mechanism derived from the two types of heterostructures, as well as different enhancements of the photocatalytic activity. This article provides insights into heterostructure photocatalysis and describes a novel way to design and fabricate high-performance semiconductor composites.

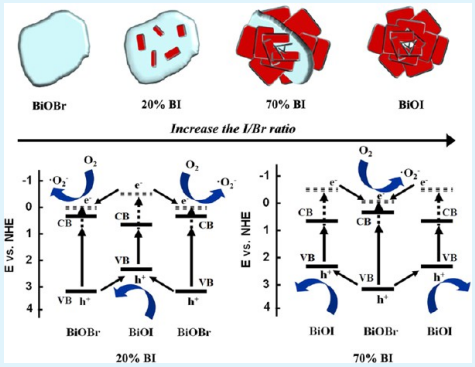

KEYWORDS: *BiOBr, BiOI, crystal structure, electronic structure, photocatalytic mechanism*

1. INTRODUCTION

Semiconductor-based photocatalysis has received increasing attention because of its promising applications in energy generation and environmental purification.[1−4] A high-performance photocatalyst system requires efficient separation and low recombination of photogenerated electrons (e^-) and holes (h^+) to ensure that the reduction and oxidation reactions can occur favorably in the conduction band (CB) and valence band (VB) of a semiconductor photocatalyst.[5]

Attempts have been made to facilitate the effective separation of photoinduced charge carriers. However, elemental doping can bring about undesirable thermal instability,[6−8] and noble-metal (Au, Pt, Ag, etc.) deposition elevates production costs.[9] In comparison, fabrication of a heterostructure based on matchable energy levels can often enhance the separation process of e^- and h^+. In addition, there are various interesting band structures in heterostructures, such as nested band structures, overlapping band structures, and completely staggered band structures. They provide many possibilities for charge transfer leading to different photocatalytic mechanisms.[10]

V–VI–VII ternary bismuth compounds BiOX (X = F, Cl, Br, I), featuring unique crystal structures consisting of $[Bi_2O_2]^{2+}$ slabs and interleaved halogen-ion layers, have lately gained considerable attention because of the efficient photocatalytic activity.[11−13] These layered crystal structures are believed to be favorable to the formation of a self-built internal static electric field, which is very beneficial to the separation and migration of photoinduced electrons and holes.[14,15] In particular, BiOBr and BiOI can respond to visible light, thus harvesting high utilization efficiency in the solar spectrum. Solid solutions such as $BiOCl_xBr_{1-x}I$,[16] $BiOBr_xI_{1-x}$,[17] and $BiOCl_xBr_{1-x}$,[18] have been synthesized to modify the crystal structure and optical properties to enhance the photocatalytic activity of single components. However, the x value varies in a small range in these alloy compounds, thereby restricting the tunable range. To further improve the photocatalytic reactivity, coupling BiOX with other types of semiconductors to construct

Received: September 23, 2014
Accepted: December 19, 2014
Published: December 19, 2014

DOI: 10.1021/am5065409
ACS Appl. Mater. Interfaces 2015, 7, 482−492

Scheme 1. Schematic Illustration of the Preparation of the BiOBr Large Plates, BiOI Nanoflakes, and BiOBr–BiOI Composite Heterostructures

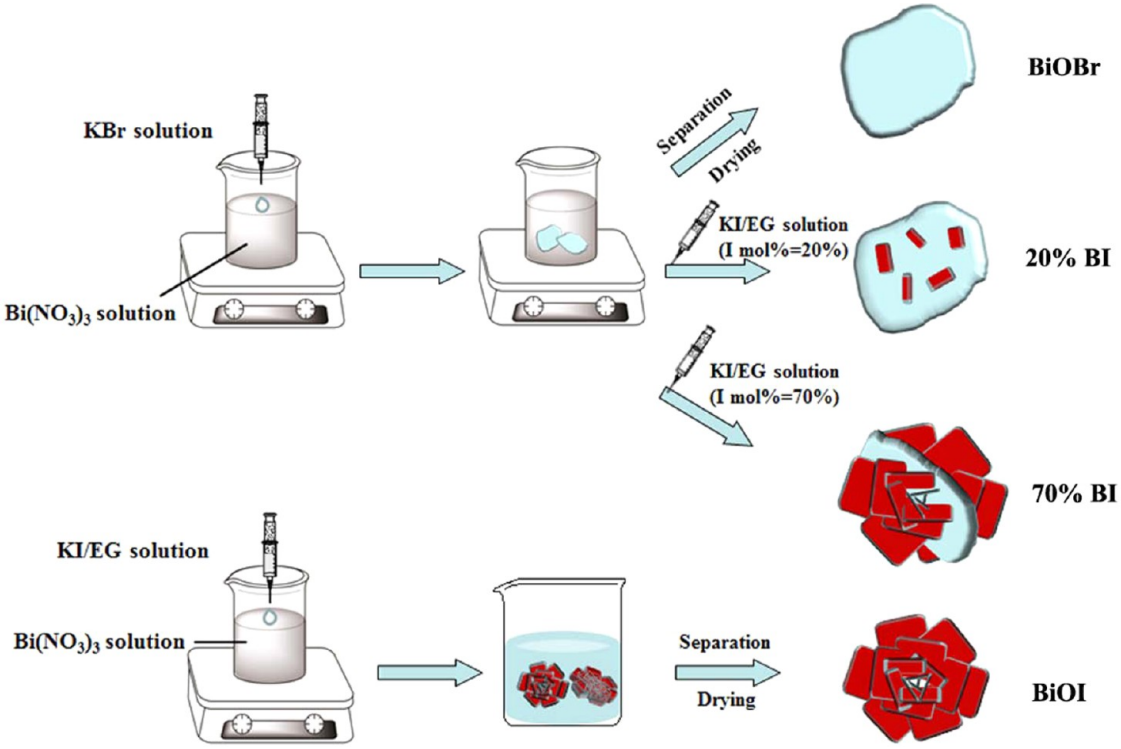

heterostructures is considered an effective strategy.[19−23] In fact, fabricating heterostructures from BiOX without the introduction of foreign semiconductors is another new approach. So far, BiOX heterojunctions including BiOCl/BiOBr,[24] BiOCl/BiOI,[25,26] and BiOBr–BiOI[27,28] have been prepared by the one-pot method, and the two components have the same microstructure. Because the microstructure of a heterojunction has a considerable influence on the photocatalytic activity, microstructural regulation of the BiOX self-heterojunctions is highly desirable, albeit challenging, to further our understanding of the photocatalytic enhancement mechanism.

In this study, we employ a facile room-temperature precipitation method to prepare multiple heterojunctions with tunable photocatalytic reactivity in full-range BiOBr–BiOI composites. Microstructure modulation can lead to two types of heterostructures with different photocatalytic mechanisms, which are responsible for the significant enhancement of the photocatalytic activity and photocurrent under visible light exposure. The formation process of the multiple heterostructures and corresponding interfacial charge-transfer mechanisms are investigated in detail.

2. EXPERIMENTAL SECTION

2.1. Synthesis of BiOBr–BiOI Composite Photocatalyst. The chemicals were of analytical grade and were used without further purification. The BiOBr–BiOI composites, pure BiOBr, and BiOI were prepared by chemical precipitation. In a typical synthesis, 1 mmol of $Bi(NO_3)_3{\cdot}5H_2O$ and 1 mmol of KBr were dissolved in 20 mL of deionized water, and 20 mL of an ethylene glycol (EG) solution containing a certain amount of KI was added dropwise. The precipitate was collected, washed repeatedly with water, and dried at 80 °C for 10 h. The as-synthesized samples were labeled as BiOBr, 5% BI, 10% BI, 20% BI, 30% BI, 40% BI, 50% BI, 60% BI, 70% BI, 80% BI, 90% BI, 95% BI, and 100% BI corresponding to the molar percentage of KI in the KI/KBr mixed solution. Pure BiOI was prepared by the same technique only replacing the KBr aqueous solution by a KI EG solution. The synthesis procedures are illustrated in Scheme 1.

2.2. Characterization. Information on phase structure of full-range BiOBr–BiOI composites were provided by X-ray diffraction (XRD) (Bruker AXS GmbH, Karlsruhe, Germany) with monochromatic Cu Kα radiation (λ = 1.5406 nm). An S-4800 scanning electron microscope (Hitachi, Tokyo, Japan) was employed to examine the microstructure and morphology of the samples, and a JEM-2100 electron microscope (JEOL, Tokyo, Japan) was used to obtain transmission electron microscopy (TEM) and high-resolution TEM (HR-TEM) images. The optical properties of the samples were studied by measuring their UV–vis absorption spectra on a Cary 5000 (Varian, Palo Alto, CA) spectrophotometer. The emission spectra were recorded on a Hitachi F-4600 fluorescence spectrophotometer.

2.3. Photocatalytic Evaluation. The photocatalytic performances of the BiOBr–BiOI full-range composites were monitored by degradation of the model dye rhodamine B (RhB) and phenol under visible light illumination (500 W, λ > 420 nm). The average light intensity was 22 mW/cm^2. First, the photocatalyst in a total amount of 50 mg was ultrasonically dispersed into 50 mL of RhB aqueous solution (3×10^{-5} mol/L) or phenol solution (10 mg/L). Prior to photoreaction, desorption–adsorption equilibrium between the dye and photocatalyst was achieved by vigorously stirring the suspension in the dark for 1 h. Then, the mixture was exposed to a 500-W Xe lamp coupled with 420-nm UV filters. At appropriate intervals, about 3 mL of the reaction suspension was withdrawn and centrifuged to remove the solid. The concentration of the supernatant liquid was measured by recording the change of characteristic bands of RhB at 554 nm and phenol at 270 nm on a UV-5500PC spectrophotometer (Shanghai Bilon Instrument Co., Ltd., Shanghai, China).

2.4. Active Species Trapping and $^{\bullet}O_2^-$ and $^{\bullet}OH$ Quantification Experiments. The active species produced during the photocatalytic reaction, including superoxide radicals ($^{\bullet}O_2^-$), hydroxyl radicals ($^{\bullet}OH$), and holes (h^+), were detected by adding 1 mM ethylenediaminetetraacetic acid disodium salt (EDTA-2Na), 1 mM benzoquinone (BQ), and 1 mM isopropanol (IPA) as scavengers.[29,30] This radical trapping process was operated the same as the former

DOI: 10.1021/am5065409
ACS Appl. Mater. Interfaces 2015, 7, 482–492

photodegradation experiment except for the presence of additional scavengers in the photoreaction system.

The amounts of $^{\bullet}O_2^-$ and $^{\bullet}OH$ generated were quantitatively inspected by nitroblue tetrazolium (NBT) transformation and terephthalic acid photoluminescence (TA-PL) probing, respectively.[31−33] NBT, which can react with $^{\bullet}O_2^-$ and displays a maximum absorbance at 260 nm, was selected to determine the amounts of $^{\bullet}O_2^-$ generated over the photocatalysts. By recording the concentration of NBT on a UV-5500PC spectrophotometer, the production of $^{\bullet}O_2^-$ was quantitatively analyzed. Upon combining with $^{\bullet}OH$, terephthalic acid (TA) is transformed into a highly fluorescent product, 2-hydroxyterephthalic acid, that can be detected on a fluorescence spectrophotometer. The production of $^{\bullet}OH$ was quantitatively resolved by monitoring the PL intensity of 2-hydroxyterephthalic acid (excitation at 315 nm). The $^{\bullet}O_2^-$ and $^{\bullet}OH$ quantification experiments were also the same as that of RhB photodegradation, only with NBT and TA, respectively, replacing the RhB.

2.5. Photoelectrochemical Measurements. Photoelectrochemical properties, including the photocurrent and electrochemical impedance spectrum, were determined using a CHI-660B electrochemical system (China) at 0.0 V with a light intensity of 1 mW/cm^2. The as-prepared samples (BiOBr, BiOI, 20% BI, and 70% BI) were coated on indium tin oxide (ITO) as the working electrode. A saturated calomel electrode (SCE) and platinum wires were utilized as the reference electrode and counter electrode, respectively. The electrolyte was 0.1 M Na_2SO_4.

2.6. Theoretical Calculations. The plane-wave ultrasoft pseudopotential method with the CASETP code was employed in this work.[34,35] The calculations were performed using the Perdew−Burke−Ernzerhof functional (PBE) formalism with an energy cutoff of 400 eV. The convergence criteria for energy and force were set to 10^{-6}/atom and 0.01 eV/A, respectively. A 2 × 2 × 2 Monkhorst−Pack *k*-point mesh was chosen for Brillouin zone integration, whereas calculations of densities of states (DOS) employed a 3 × 3 × 3 *k*-point mesh.

3. RESULTS AND DISCUSSION

3.1. Characterization of Photocatalysts. The X-ray diffraction (XRD) patterns of the full-range BiOBr−BiOI composites, BiOBr, and BiOI are presented in Figure 1, and all of the diffraction peaks can be indexed to the tetragonal phases of BiOBr (JCPDS file 09-0393) and BiOI (JCPDS file 10-0445). The absence of other impurity peaks indicates that the as-synthesized BiOBr and BiOI were pure phases.[13] For all of the BiOBr−BiOI composites, the characteristic (110) peak of BiOBr and (102) peak of BiOI coexist in the XRD patterns, demonstrating the formation of the full-range BiOBr−BiOI composites without the presence of $BiOBr_xI_{1-x}$ solid solutions. The intensity of the diffraction peaks of one component increased gradually as that of the counterpart diminished. Thus, XRD demonstrates the successful synthesis of the full-range BiOBr−BiOI composites.

The microstructures of BiOBr, BiOI, and the full-range BiOBr−BiOI composites were investigated by scanning electron microscopy (SEM), as shown in Figure 2. For the pristine BiOBr, the direct and fast reaction of $Bi(NO_3)_3{\cdot}5H_2O$ and KBr in aqueous solutions results in the formation of irregularly large plates of BiOBr with sizes of several hundred nanometers or micrometers, as revealed in Figure 2a. Figure 2l shows that the BiOI product consists of uniformly hierarchical microspheres assembled by plenty of tiny nanoflakes. In the preparation process of BiOI microspheres, ethylene glycol (EG) plays a critical role. Because of the excellent chelating ability of EG, alkoxides $Bi(OCH_2CH_2OH)^{2+}$ can form as a result of the coordination of Bi^{3+} ions with EG, which allows $Bi(NO_3)_3$ to be completely dissolved to form a clear and highly

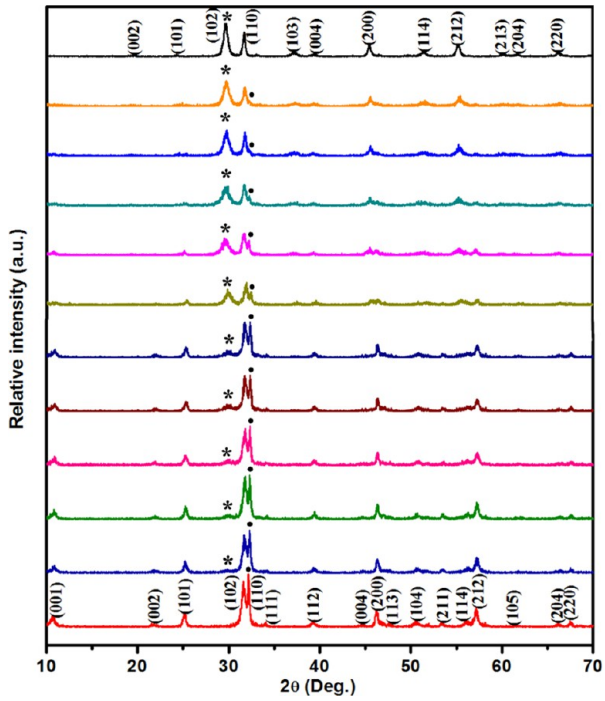

Figure 1. XRD patterns of BiOBr, 5% BI, 10% BI, 20% BI, 30% BI, 40% BI, 50% BI, 60% BI, 70% BI, 80% BI, 90% BI, and BiOI (from bottom to top).

homogeneous solution. In view of its poor solubility, BiOI was believed to precipitate out simultaneously as the KI started to react with $Bi(OCH_2CH_2OH)^{2+}$ in the EG solution. Thus, on one hand, EG acts as an excellent solvent. More importantly, it can restrict the growth of BiOI crystals, which results in the tiny size of BiOI nanosheets. These tiny nanosheets then assemble together to form three-dimensional microspheres of BiOI to minimize the surface energy (Figure 2l). Based on the two different microstructures of BiOBr and BiOI, BiOBr−BiOI composites with quite different morphologies can be obtained by controlling the contents of the constituents, as revealed in Figure 2b−k. It can be seen that all of the BiOBr−BiOI heterostructural composites contained the above two phases. It is also important to note that the microstructure of the BiOBr−BiOI composites can be tuned in an orderly manner by changing the relative contents of the two components. When the BiOBr content was large, such as in 5% BI to 40% BI (Figure 2b−f), the products had large-plate structures with thin nanosheets of BiOI embedded, as illustrated by 20% BI in Scheme 1. When the BiOI molar ratio was greater than 50% (Figure 2h−k), the products formed three-dimensional microspheres composed of tiny BiOI nanoflakes and a small quantity of large BiOBr plates, as illustrated by 70% BI in Scheme 1. The distinct microstructures and compositions of the BiOBr−BiOI composites can lead to different separation and transfer mechanisms of the photoinduced charge carriers in the photoreaction process.

The microstructures of BiOBr, BiOI, and the BiOBr−BiOI composites were further studied by transmission electron microscopy (TEM). Panels a and b of Figure 3 reveal the irregular large plates of BiOBr and the three-dimensional hierarchical microspheres of BiOI, respectively. To obtain a better understanding of the BiOBr−BiOI heterostructure, high-resolution TEM (HR-TEM) images of 20% BI and 70% BI are displayed in panels c and d, respectively, of Figure 3. The fast

DOI: 10.1021/am5065409
ACS Appl. Mater. Interfaces 2015, 7, 482−492

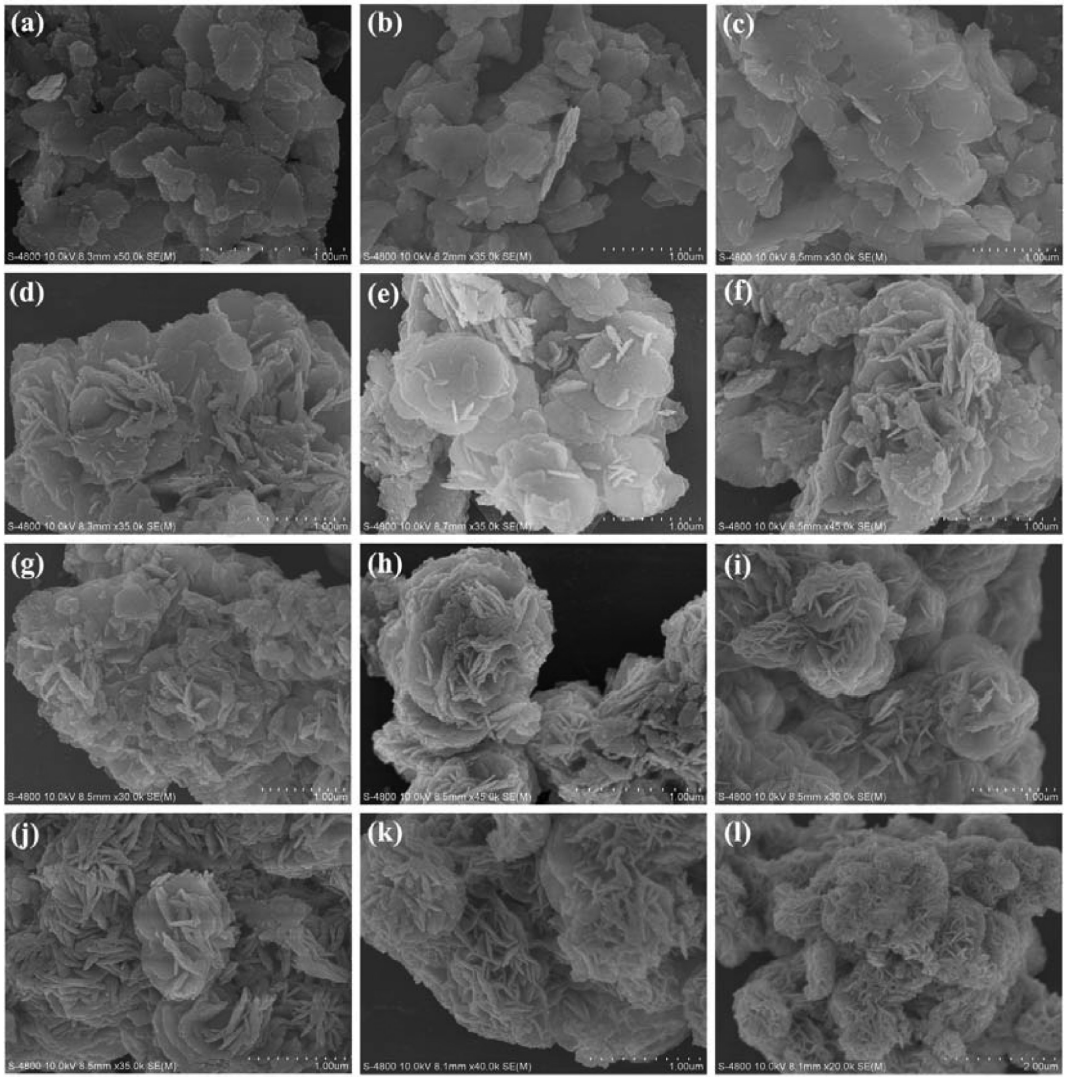

Figure 2. SEM images of (a) BiOBr, (b) 5% BI, (c) 10% BI, (d) 20% BI, (e) 30% BI, (f) 40% BI, (g) 50% BI, (h) 60% BI, (i) 70% BI, (j) 80% BI, (k) 90% BI, and (l) BiOI.

Fourier transform (FFT) patterns of BiOBr (Figure 3e) and BiOI (Figure 3h) confirm the single-crystal nature. The HR-TEM and reduced FFT images (Figure 3f,g) of the 20% BI sample show that there are two sets of lattice fringes with intervals of 0.277 and 0.269 nm that can be indexed to the (110) lattice plane of tetragonal BiOBr and the (111) crystal plane of BiOI, respectively. Figure 3d shows that the HR-TEM image of 70% BI consisted of two different lattice fringes with intervals of 0.277 and 0.282 nm that are in good agreement with the spacings of the corresponding (110) facets of BiOBr and BiOI, respectively. These results further corroborate the synthesis of BiOBr−BiOI heterostructures and are consistent with the XRD and SEM results.

Figure 4a displays UV−vis diffuse reflection spectra of the as-prepared samples, and all of the samples exhibit light absorption in the visible range. BiOBr can absorb only light with wavelengths shorter than 435 nm, whereas the absorption edge of BiOI is approximately 680 nm. The absorption edges of all of the BiOBr−BiOI composites are between those of BiOBr and BiOI and gradually extend to longer wavelengths with increasing BiOI content. The corresponding band gaps can be obtained from the equation $\alpha h\nu = A(h\nu - E_g)^{n/2}$, where α, $h\nu$, E_g, and A are the optical absorption coefficient, photonic energy, band gap, and proportionality constant, respectively.[36] Herein, the n value for BiOBr and BiOI was selected to be 4, because BiOBr and BiOI are indirect-band-gap-transition semiconductors. According to plots of the square root of absorption versus energy, the band gaps of BiOBr and BiOI were determined to be 2.67 and 1.72 eV, respectively (Figure 4b). Because the heterostructure construction was closely related to the band potentials of the components, the edge positions of the conduction band (CB) and valence band (VB) of BiOBr and BiOI were estimated by the expressions[36]

$$E_{VB} = X - E_e + 0.5E_g \quad (1)$$

$$E_{CB} = E_{VB} - E_g \quad (2)$$

where E_{VB} and E_{CB} are the valence band (VB) and conduction band (CB) potentials, respectively; E_e (~4.5 eV) is the energy of free electrons on the hydrogen scale; E_g is the band gap; and X is the electronegativity of the semiconductor (geometric average of the absolute electronegativities of the constituent atoms). The E_{CB} values of BiOBr and BiOI were calculated to

DOI: 10.1021/am5065409
ACS Appl. Mater. Interfaces 2015, 7, 482−492

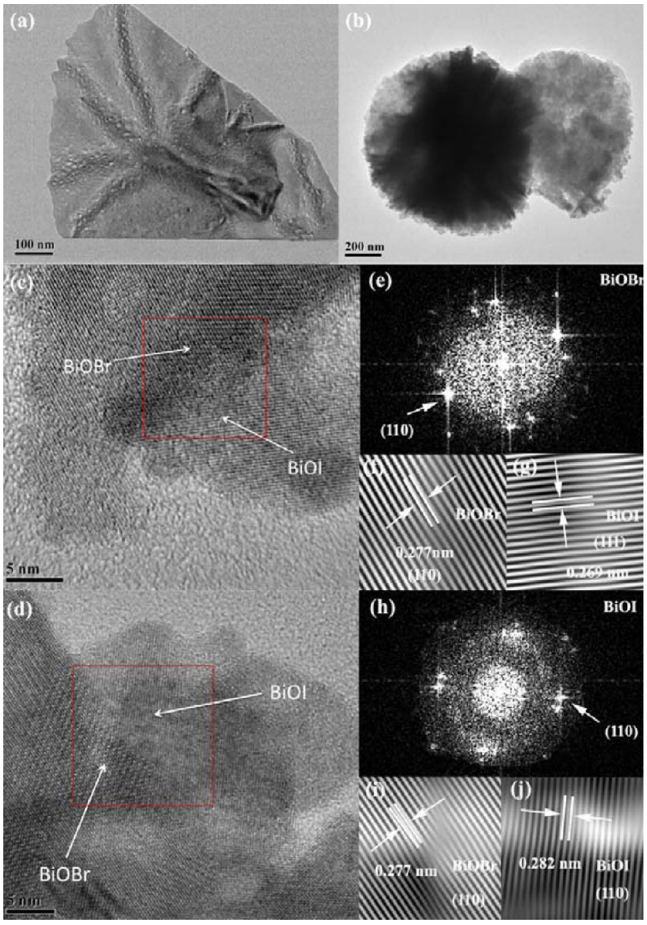

Figure 3. (a,b) TEM images of (a) BiOBr and (b) BiOI. (c,d) HRTEM images of (c) 20% BI and (d) 70% BI. (e) Fast Fourier transform (FFT) patterns and (f,g) inverse FFT patterns with the lattice fringe of patterns of 20% BI. (h) FFT patterns and (i,j) inverse FFT patterns with the lattice fringe of patterns of 70% BI.

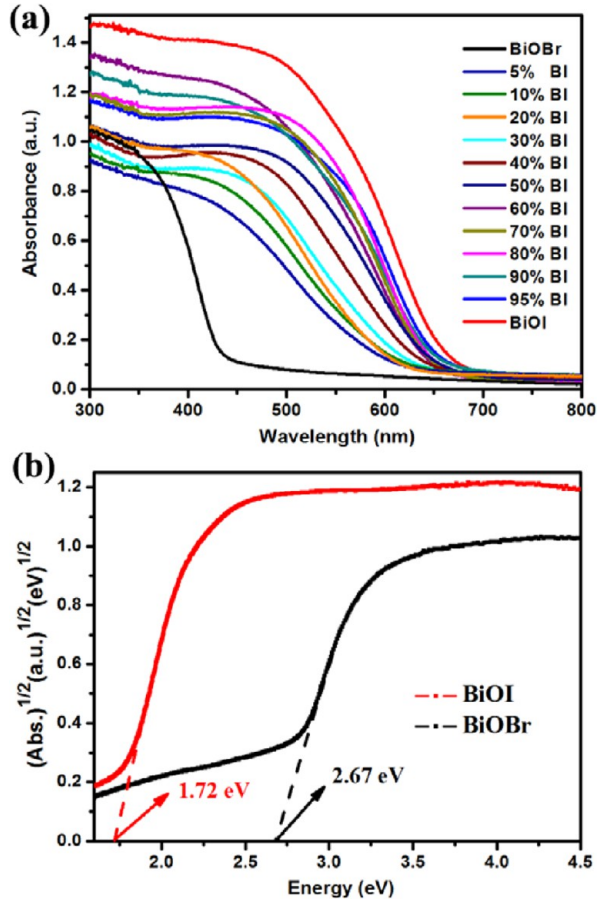

Figure 4. (a) UV−vis diffuse reflectance spectra of full-range BiOBr−BiOI composites. (b) Band gap energies of BiOBr and BiOI.

be 0.34 and 0.58 eV, respectively, and the E_{VB} values of BiOBr and BiOI were estimated to be 3.01 and 2.30 eV, respectively.

3.2. Calculations on BiOBr and BiOI Photocatalysts. The electronic band structures of BiOBr and BiOI are illustrated in Figure 5a,b. Both compounds exhibit the same optical transition type. As indicated, the lowest unoccupied states are located at the Z point, and the highest occupied states are at the R point, confirming that both BiOBr and BiOI are indirect-band-gap semiconductors. The indirect band gaps of BiOBr and BiOI were calculated to be 2.17 and 1.65 eV, respectively, which are slightly smaller than the experimental band energies from UV−vis diffuse reflection spectroscopy (DRS). This is because the band gaps derived from DFT calculations are usually underestimated.[37] Moreover, a relatively larger dispersion was observed for the CB hybridized orbitals of BiOBr, implying that the photoinduced electrons of BiOBr have a higher mobility than those of BiOI. This phenomenon bodes well for the transport of photoexcited charge carriers.

Figure 5c,d presents the imaginary dielectric functions along the different crystallographic axes.[38] It can be clearly observed that light absorption by BiOI is extended to a lower energy range than that by BiOBr, indicating that BiOI can absorb light with shorter wavelengths, which is consistent with the electronic band structures. They exhibit relatively strong absorbance along the x or y direction in the UV−visible light range and along the z axis in the super-high-energy range. As shown in Figure 5e, infinite $[Bi_2O_2]^{2+}$ slabs stretch along the x−y plane and stack along the z axis, with halogen ions interleaved in the space between the cationic layers to form the three-dimensional crystal structures of BiOX. That is, the $[Bi_2O_2]^{2+}$ layers in BiOBr/I are mainly responsible for visible light absorption in the photocatalytic process.

The total and partial densities of states of BiOBr and BiOI are displayed in Figure 6a,b. The contributions near the Fermi surface mainly result from the p orbitals of the atoms. There is no significant difference in the electron densities of BiOBr and BiOI. The valence band maximum (VBM) is composed of the Br 4p or I 5p orbital and the O 2p orbitals, and the conduction band minimum (CBM) mainly consists of the Bi 6p orbital and small amount of O 2p orbitals. Separate occupation of the orbitals from cationic and anionic layers in the CB and VB favors separation of the photogenerated electrons and holes.

3.3. Photocatalytic Reactivity. The photocatalytic activities of the as-synthesized BiOBr, BiOI, and full-range BiOBr−BiOI composites were evaluated by decomposing RhB under visible light irradiation (λ > 420 nm). The degradation curves of the BiOBr−BiOI composites with 5−50% BiOI and 50−95% BiOI are shown in Figures S1 and S2 (Supporting Information), respectively. Generally, the photocatalytic decomposition of RhB follows pseudo-first-order kinetics. As shown in Figure 7a, all of the BiOBr−BiOI composite photocatalysts in the 5−50% range exhibited photocatalytic activities superior to those of pristine BiOBr and BiOI, demonstrating that effective charge transfer indeed occurred between the

DOI: 10.1021/am5065409
ACS Appl. Mater. Interfaces 2015, 7, 482−492

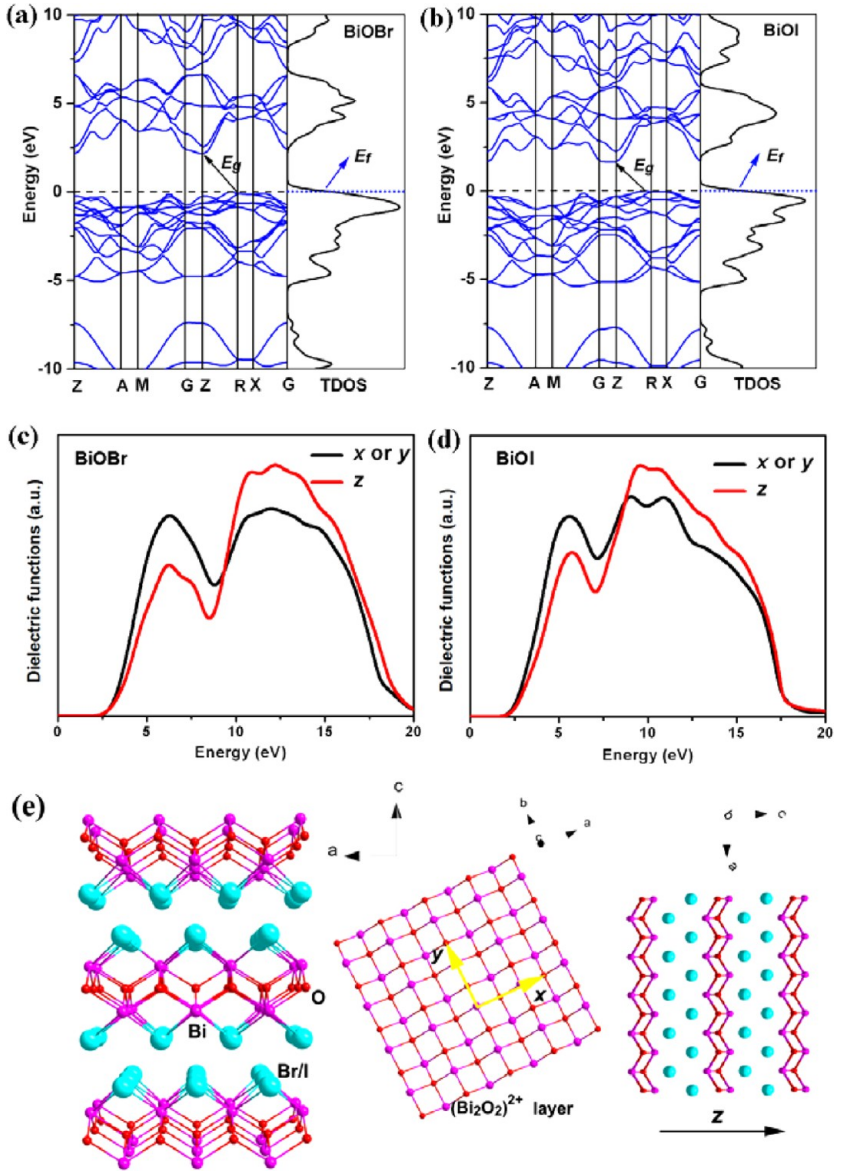

Figure 5. (a,b) Electronic band structures of (a) BiOBr and (b) BiOI. (c,d) Calculated imaginary dielectric functions versus energy of (c) BiOBr and (d) BiOI. (e) Crystal structures of BiOBr/I along different directions.

BiOBr and BiOI matrixes. In particular, 20% BI exhibited the highest photocatalytic efficiency with an apparent rate constant 2.52 h^{-1}, translating into a 90% degradation rate for RhB after visible light irradiation for 1 h. This value is 4.2 and 9.4 times higher than those of BiOBr and BiOI, respectively. When the content of BiOI was less than 20%, the amount of BiOI was not sufficient to construct the most effective heterojunction structure between BiOBr and BiOI for the separation and transfer of photogenerated electron−hole pairs. Hence, the photocatalytic activity of the BiOBr−BiOI composites gradually increased with increasing the amount of BiOI in the range of 0−20%. Nevertheless, excess BiOI amounts (20−50%) would reduced the photocatalytic activity of the BiOBr−BiOI composites because of the lower degradation efficiency of BiOI compared to BiOBr. Interestingly, another optimal photocatalytic activity was observed for 70% BI in the 50−95% range. It exhibited a higher photodegradation rate, approximately 1.9 and 4.1 times those of BiOBr and BiOI, respectively. The heterostructures formed between BiOBr and BiOI result in optimal photocatalytic performance for different composition ranges, suggesting that there might be two photocatalytic mechanisms that are closely related to the microstructure.

To exclude the effect of dye sensitization, we selected the colorless organic contaminant phenol as a degradation model to further investigate the photocatalytic activity. Phenol is a typically colorless pollutant that is very difficult to degrade. As revealed in Figure 7c, only 45% and 34% of phenol can be degraded over pristine BiOBr and BiOI, respectively, within 10 h. Comparatively, 20% BI and 70% BI can decompose 75% and 60% of phenol, respectively, in the same period. Thus, the greatly enhanced photocatalytic activities of BiOBr−BiOI composites were also confirmed for phenol degradation. Meanwhile, the photocatalytic degradation order was also consistent with that of RhB removal. The time-resolved spectral change of phenol over 20% BI (Figure 7d) also revealed that the characteristic absorption band of phenol at 270 nm gradually decreased with as the illumination time was extended.

DOI: 10.1021/am5065409
ACS Appl. Mater. Interfaces 2015, 7, 482−492

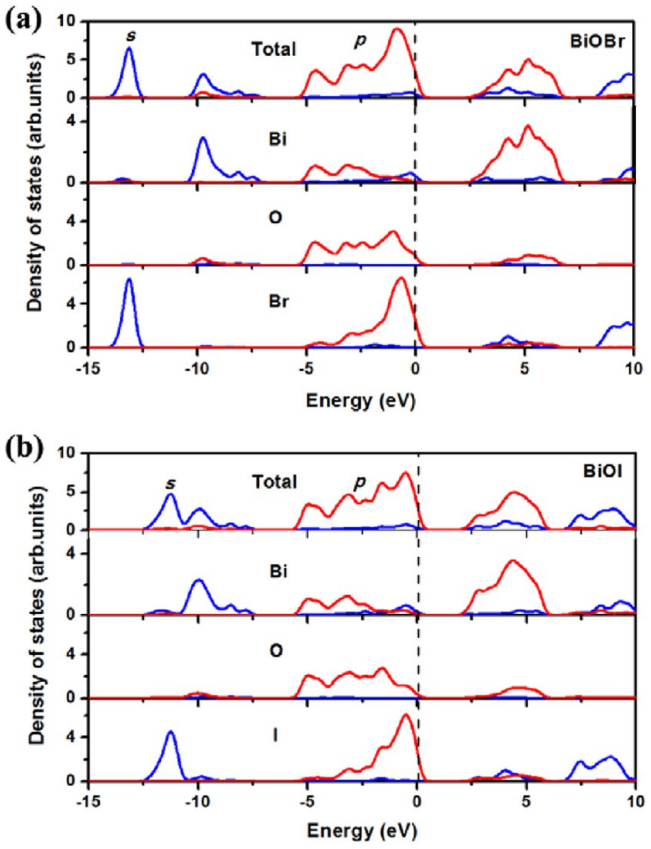

Figure 6. Total and partial densities of states of (a) BiOBr and (b) BiOI.

Photocurrent measurements were performed to further investigate the photocatalytic performance, which can be correlated with the generation and transfer of photoexcited charge carriers in the photocatalytic process.[39] Both 20% BI and 70% BI exhibited enhanced photocurrent responses compared to the pristine samples. As shown in Figure 8a, 20% BI exhibited photocurrent responses that were 11.6 and 3.3 times higher than those of BiOBr and BiOI, respectively. Figure 8b shows that the photocurrent density of 70% BI was 6.7 and 1.8 times those of BiOBr and BiOI, respectively. These photocurrent efficiencies are consistent with the degrees of photocatalytic activity. Hence, in the cases of 20% BI and 70% BI, the separation and transfer efficiency of the photoinduced electron−hole pairs was improved by the interfacial interactions between BiOBr and BiOI.

3.4. Investigation of the Mechanism of Photocatalytic Activity Enhancement. Electrochemical impedance spectroscopy (EIS) and photoluminescence (PL) spectroscopy were utilized to investigate the charge migration processes and recombination rates of the photocatalysts, as these are two crucial factors for photocatalytic activity.[40,41] Figure 9a,b shows the EIS spectra obtained at the interface between the electrolyte and photocatalysts. The diameters of the arc radii of 20% BI and 70% BI are clearly much smaller than those of BiOBr and BiOI, indicating a higher efficiency of charge transfer on the surface of the 20% BI and 70% BI photocatalysts. The PL spectra obtained from BiOBr, BiOI, and the BiOBr−BiOI composites are displayed in Figure 9c,d. The 20% BI and 70% BI samples exhibited lower PL emission intensities compared to pristine BiOBr, pristine BiOI, and the other composites, revealing a lower recombination of photogenerated electrons and holes

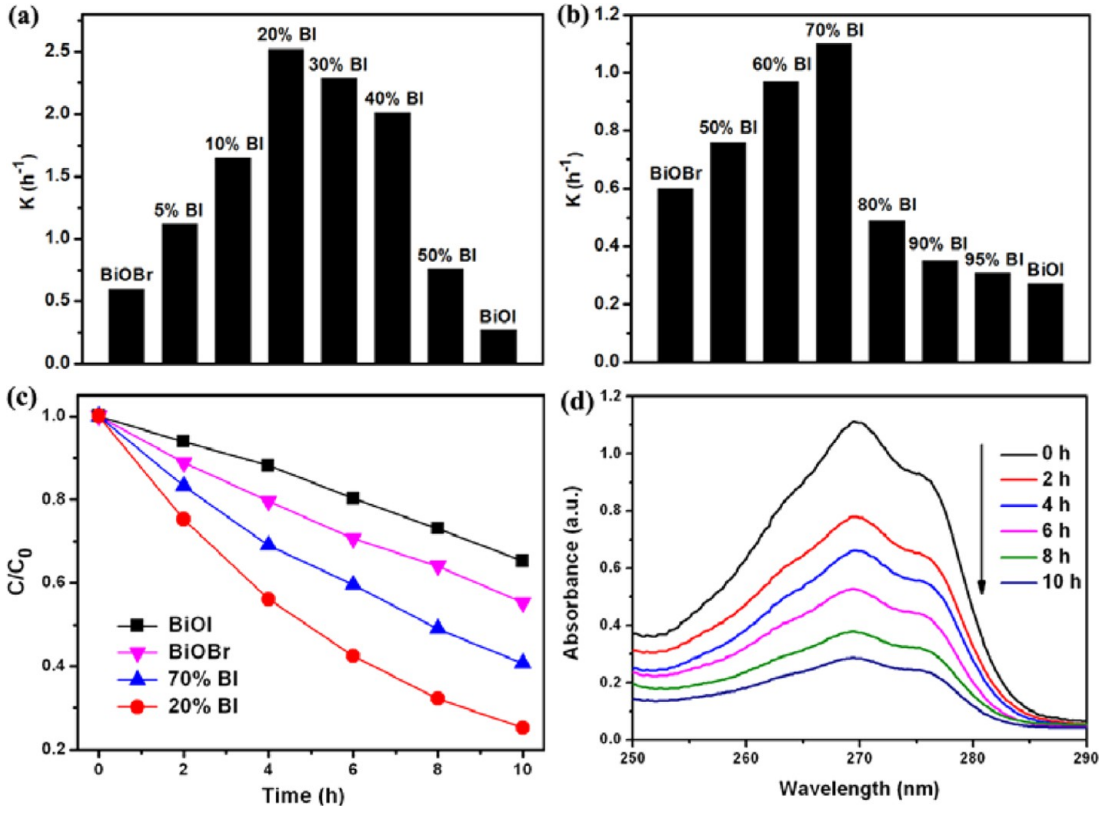

Figure 7. Apparent rate constants for photodecomposition of RhB over (a) BiOBr, BiOI, and 5−50% BiOBr−BiOI composites and (b) BiOBr, BiOI, and 50−95% BiOBr−BiOI composites under visible light irradiation ($\lambda > 420$ nm). (c) Photodegradation curves of phenol over BiOBr, BiOI, 20% BI, and 70% BI. (d) Time-resolved spectral changes of phenol over 20% BI.

DOI: 10.1021/am5065409
ACS Appl. Mater. Interfaces 2015, 7, 482−492

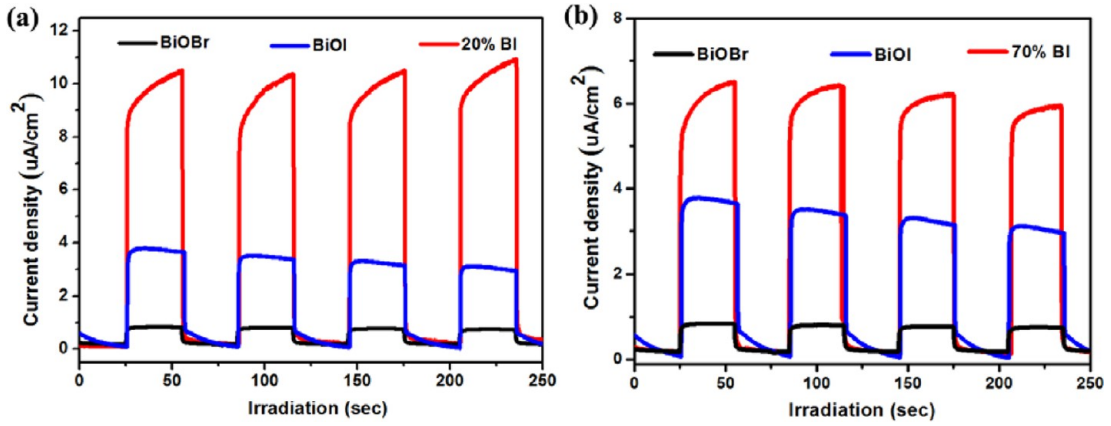

Figure 8. Transient photocurrent densities of (a) BiOBr, BiOI, and 20% BI and (b) BiOBr, BiOI, and 70% BI electrodes with light on/off cycles under visible light irradiation (λ > 420 nm, [Na_2SO_4] = 0.1 M).

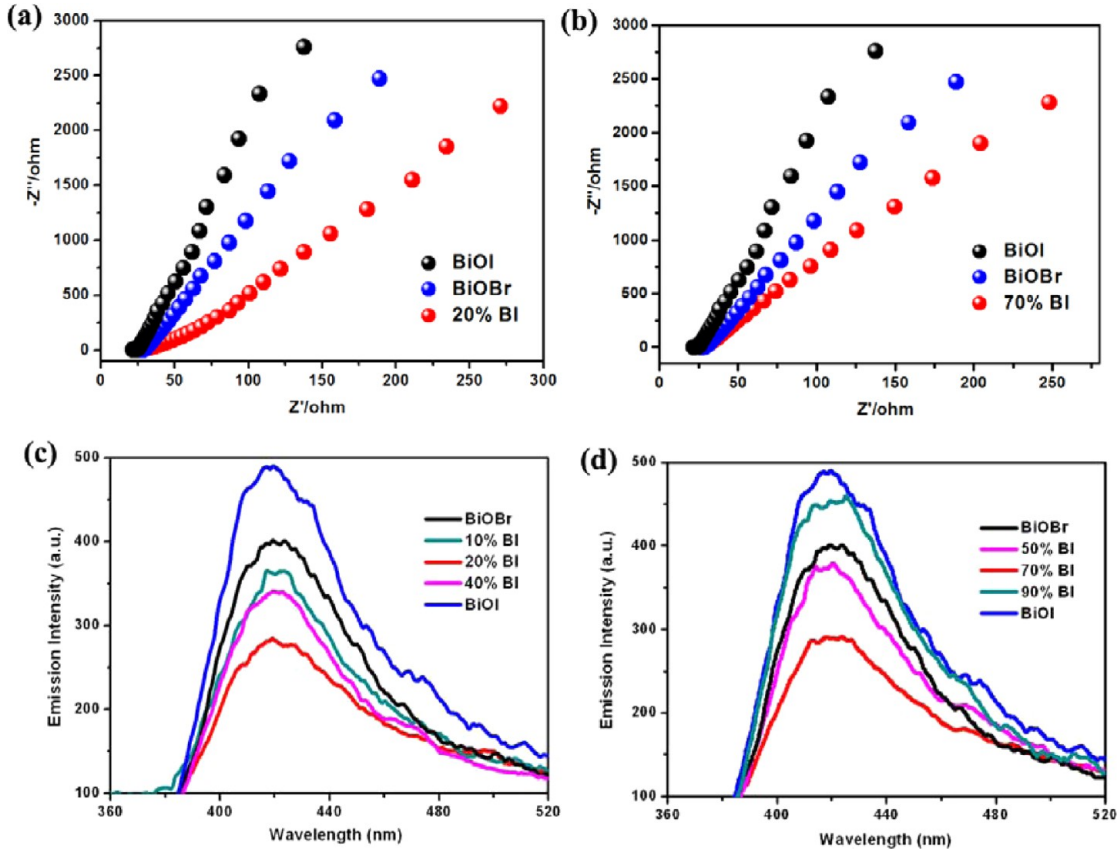

Figure 9. (a,b) EIS Nynquist plots of BiOBr, BiOI, 20% BI, and 70% BI under visible light irradiation (λ > 420 nm, [Na_2SO_4] = 0.1 M). (c,d) PL spectra of BiOBr, BiOI, 10% BI, 20% BI, 40% BI, 50% BI, 70% BI, and 90% BI.

and a longer lifetime of charge carriers in 20% BI and 70% BI. The EIS and PL results demonstrate that the heterostructures fabricated based on microstructural modulation facilitated separation and inhibited recombination of the photoinduced electron−hole pairs, thereby giving rise to an improved photocatalytic reactivity.

To detect the active species in the photooxidation process for 20% BI and 70% BI, the molecular detectors ethylenediaminetetraacetic acid disodium salt (EDTA-2Na), benzoquinone (BQ), and isopropanol (IPA) were introduced to quench holes (h^+), superoxide radicals ($^\bullet O_2^-$), and hydroxyl radicals ($^\bullet OH$), respectively.[29,30] As shown in Figure 10a,b, IPA (scavenger of $^\bullet OH$) had almost no effect on RhB degradation for both 20% BI and 70% BI, indicating that no $^\bullet OH$ radicals were generated. Nevertheless, a distinct influence was observed when BQ and EDTA-2Na were introduced. For 20% BI, as shown in Figure 10a, a significant decrease was observed after the addition of BQ (scavenger of $^\bullet O_2^-$), demonstrating that $^\bullet O_2^-$ is the main active species in the RhB photooxidation process. RhB degradation was moderately mitigated in the presence of EDTA-2Na (scavenger of h^+), suggesting that modest amounts of h^+ are involved in the RhB decomposition process. In contrast, in the photodegradation using 70% BI, h^+ was found to play a dominant role and $^\bullet O_2^-$ to play a secondary role, as EDTA-2Na

DOI: 10.1021/am5065409
ACS Appl. Mater. Interfaces 2015, 7, 482−492

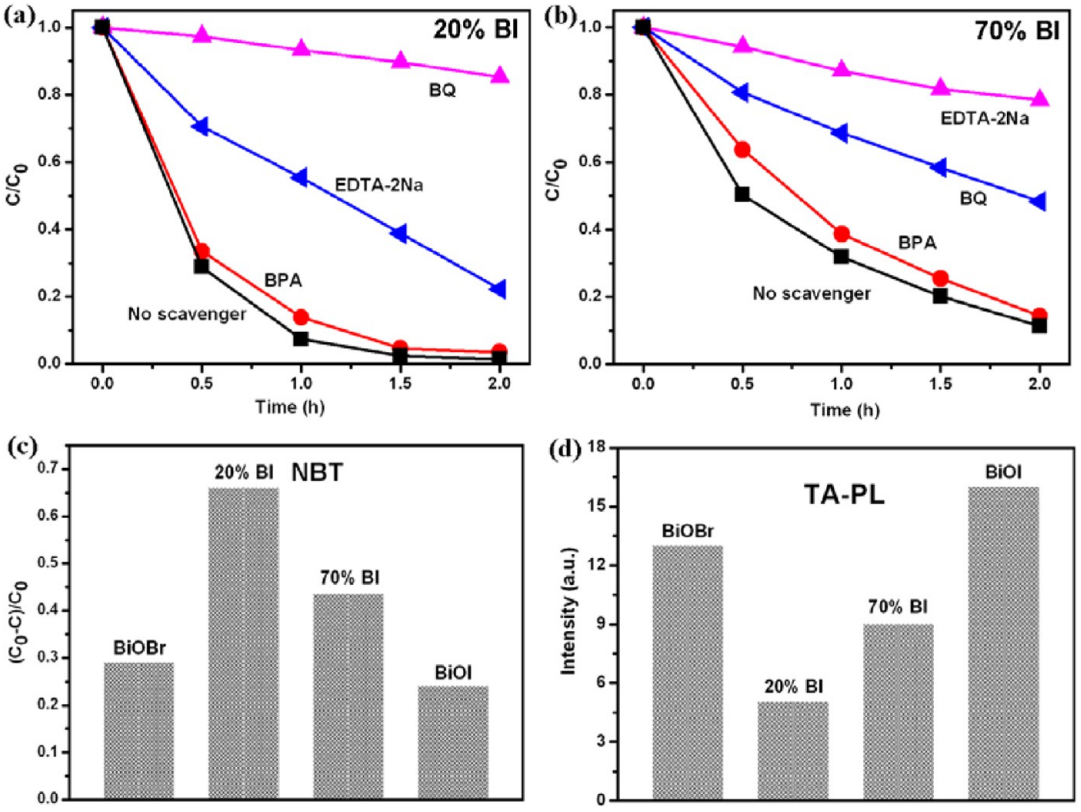

Figure 10. (a,b) Reactive species trapping experiments over (a) 20% BI and (b) 70% BI heterostructures. (c) Nitroblue tetrazolium (NBT) transformation efficiencies and (d) hydroxyterephthalic acid (TAOH) fluorescence intensities of BiOBr, BiOI, 20% BI, and 70% BI.

had a more positive effect than BQ in inhibiting RhB degradation. The active-species trapping experiments thus revealed that the 20% BI and 70% BI heterostructures have different photocatalytic mechanisms pertaining to RhB degradation.

To verify the results obtained from the aforementioned active-species trapping tests and quantitatively compare the amounts of radicals generated on 20% BI and 70% BI, $^{\bullet}O_2^-$ and $^{\bullet}OH$ production was quantified after visible light irradiation ($\lambda > 420$ nm) for 1 h by the nitroblue tetrazolium (NBT, detection agent of $^{\bullet}O_2^-$) transformation and terephthalic acid photoluminescence (TA-PL) probing techniques.[31−33,42] As shown in Figure 10d, the fluorescence intensity of hydroxyterephthalic acid (TAOH) over BiOBr, BiOI, 20% BI, and 70% BI was negligible, indicating that no $^{\bullet}OH$ was generated from the h^+. These results are consistent with those obtained from the radical trapping measurements. Figure 10c along with the time-resolved absorption spectra of NBT (Figure S3, Supporting Information) present the transformation percentage of NBT catalyzed by the four samples, showing that 20% BI and 70% BI were more efficient in generating $^{\bullet}O_2^-$ than the pristine samples. The difference can be attributed to the effective interfacial transfer of charge carriers at the BiOBr−BiOI heterostructures. Moreover, the NBT conversion percentage of 20% BI was up to 67%, which far exceeded those of BiOBr, BiOI, and 70% BI. The NBT transformation further confirms the radical trapping results and suggests that the 20% BI heterostructure can more easily produce $^{\bullet}O_2^-$ than the 70% BI one.

According to the above results, two possible photocatalytic mechanisms based on the band structures and microstructures of the catalysts are proposed for 20% BI and 70% BI, as illustrated in Figure 11.[43] The nested band energy levels of BiOBr (E_{CB} = 0.34 eV, E_{VB} = 3.01 eV) and BiOI (E_{CB} = 0.58 eV, E_{VB} = 2.30 eV) do not favor transfer of photoexcited electrons and holes between the two bulk photocatalysts. Nevertheless, under visible light irradiation at energies below 2.95 eV ($\lambda >$ 420 nm), the electrons of BiOBr can be excited and then transit from the VB position of BiOBr to the position of 0.06 eV in the CB of BiOBr. Similarly, the electrons of BiOI can jump to the potential of −0.65 eV in the CB of BiOI. The altered band structures between BiOBr and BiOI with staggered energy levels enable effective interfacial transfer of the photoinduced charges. With regard to 20% BI, the electrons of the BiOI nanoflakes can easily jump to the CB and then be injected into the less negative CB of the surrounding BiOBr. The large number of large BiOBr plates provides an excellent platform to transfer electrons, consequently facilitating the reaction between electrons and O_2 molecules adsorbed on the surface of the photocatalyst to produce more $^{\bullet}O_2^-$. Meanwhile, the photoexcited holes (h^+) in the VB of BiOBr are transferred to the VB of BiOI because of the more positive VB of the BiOBr and interfacial interactions. On account of the limited surface area of BiOI, a smaller number of h^+ can participate in oxidization, and hence, $^{\bullet}O_2^-$ plays the major role in RhB degradation in 20% BI. On the contrary, in 70% BI, the photogenerated electrons accumulate in the CB of BiOBr because of interfacial charge transfer. As the BiOBr plates are embedded in the BiOI hierarchical microspheres, only a small fraction of $^{\bullet}O_2^-$ can be generated. The photoinduced holes of BiOBr migrate to the VB of the outer BiOI and react directly with RhB. Therefore, in 70% BI, h^+ plays a greater role in RhB decomposition than $^{\bullet}O_2^-$. All in all, the two types of heterostructures with different photocatalytic mechanisms are fabricated in 20% BI and 70% BI based on the different microstructures and are responsible for the enhanced photocatalytic activity.

DOI: 10.1021/am5065409
ACS Appl. Mater. Interfaces 2015, 7, 482−492

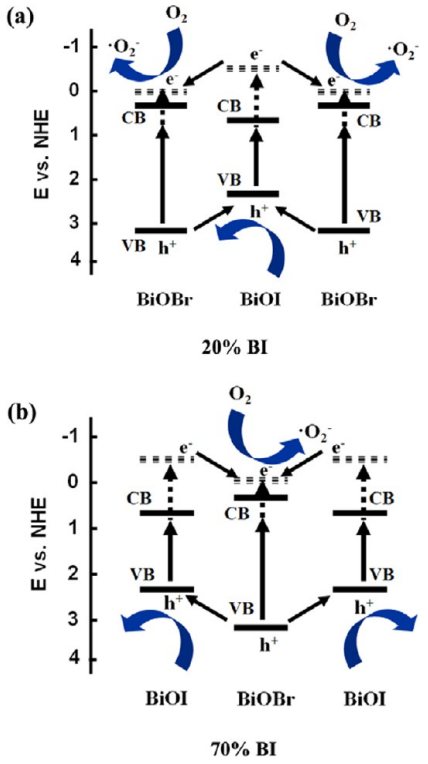

Figure 11. Schematic diagrams with different charge-transfer mechanisms of (a) 20% BI and (b) 70% BI heterostructures under visible light irradiation.

4. CONCLUSIONS

A room-temperature precipitation technique was employed to prepare multiple heterojunctions with tunable photocatalytic reactivities in full-range BiOBr–BiOI composites. Microstructural modulation effectively adjusts the visible-light-driven photocatalytic performance, producing diverse photocatalytic activity enhancements pertaining to the degradation of organic dye and photocurrent generation. Two types of charge-transfer mechanisms exist for the multiple heterostructures in the full-range BiOBr–BiOI composites, according to reactive species trapping, nitroblue tetrazolium transformation, and terephthalic acid photoluminescence experiments. Electrochemical impedance spectroscopy and photoluminescence spectroscopy confirm the promoted separation and inhibited recombination of electron–hole pairs in the heterostructures. These factors are responsible for the markedly enhanced photocatalytic avtivity of the composites, and this study presents a new direction for the design of highly efficient heterostructure photocatalysts.

■ ASSOCIATED CONTENT

Supporting Information

Degradation curves of RhB over BiOBr, BiOI, and BiOBr–BiOI composites; absorption spectra of NBT over BiOBr, BiOI, 20% BI, and 70% BI. This material is available free of charge via the Internet at http://pubs.acs.org.

■ AUTHOR INFORMATION

Corresponding Authors

*Tel.: +86-10-82322247. E-mail: hhw@cugb.edu.cn.
*Tel.: +86-10-82322247. E-mail: zyh@cugb.edu.cn.

Notes

The authors declare no competing financial interest.

■ ACKNOWLEDGMENTS

This work was supported by the National Natural Science Foundation of China (Grants No. 51302251, No. 51172245, No. 51322213), the Fundamental Research Funds for the Central Universities (2652013052), and the National High Technology Research and Development Program (863 Program 2012AA06A109) of China, as well as City University of Hong Kong Applied Research Grant 9667085.

■ REFERENCES

(1) Yu, J. G.; Low, J. X.; Xiao, W.; Zhou, P.; Jaroniec, M. Enhanced Photocatalytic CO_2-Reduction Activity of Anatase TiO_2 by Coexposed {001} and {101} Facets. *J. Am. Chem. Soc.* **2014**, *136*, 8839–8842.
(2) Shang, L.; Bian, T.; Zhang, B.; Zhang, D. H.; Wu, L. Z.; Tung, C. H.; Yin, Y. D.; Zhang, T. R. Graphene-Supported Ultrafine Metal Nanoparticles Encapsulated by Mesoporous Silica: Robust Catalysts for Oxidation and Reduction Reactions. *Angew. Chem., Int. Ed.* **2014**, *53*, 250–254.
(3) Wei, H. G.; Ding, D. W.; Yan, X. R.; Guo, J.; Shao, L.; Chen, H. R.; Sun, L. Y.; Colorado, H. A.; Wei, S. Y.; Guo, Z. H. Tungsten Trioxide/Zinc Tungstate Bilayers: Electrochromic Behaviors, Energy Storage and Electron Transfer. *Electrochim. Acta* **2014**, *132*, 58–66.
(4) Wang, X.; Xu, Q.; Li, M. R.; Shen, S.; Wang, X. L.; Wang, Y. C.; Feng, Z. C.; Shi, J. Y.; Han, H. X.; Li, C. Photocatalytic Overall Water Splitting Promoted by an α–β Phase Junction on Ga_2O_3. *Angew. Chem., Int. Ed.* **2012**, *51*, 13089–13092.
(5) Tong, H.; Ouyang, S. X.; Bi, Y. P.; Umezawa, N.; Oshikiri, M.; Ye, J. H. Nano-photocatalytic Materials: Possibilities and Challenges. *Adv. Mater.* **2012**, *24*, 229–251.
(6) Feng, N. D.; Wang, Q.; Zheng, A. M.; Zhang, Z. F.; Fan, J.; Liu, S. B.; Amoureux, J. P.; Deng, F. Understanding the High Photocatalytic Activity of (B, Ag)-Codoped TiO_2 under Solar-Light Irradiation with XPS, Solid-State NMR, and DFT Calculations. *J. Am. Chem. Soc.* **2013**, *135*, 1607–1616.
(7) Zhang, L. W.; Man, Y.; Zhu, Y. F. Effects of Mo Replacement on the Structure and Visible-Light-Induced Photocatalytic Performances of Bi_2WO_6 Photocatalyst. *ACS Catal.* **2011**, *1*, 841–848.
(8) Jiang, J.; Zhang, L. Z.; Li, H.; He, W. W.; Yin, J. J. Self-Doping and Surface Plasmon Modification Induced Visible Light Photocatalysis of BiOCl. *Nanoscale* **2013**, *5*, 10573–10581.
(9) Linic, S.; Christopher, P.; Ingram, D. B. Plasmonic-Metal Nanostructures for Efficient Conversion of Solar to Chemical Energy. *Nat. Mater.* **2011**, *10*, 911–921.
(10) Wang, H. L.; Zhang, L. S.; Chen, Z. G.; Hu, J. Q.; Li, S. J.; Wang, Z. H.; Liu, J. S.; Wang, X. C. Semiconductor Heterojunction Photocatalysts: Design, Construction, and Photocatalytic Performances. *Chem. Soc. Rev.* **2014**, *43*, 5234–5244.
(11) Cheng, H. F.; Huang, B. B.; Dai, Y. Engineering BiOX (X = Cl, Br, I) Nanostructures for Highly Efficient Photocatalytic Applications. *Nanoscale* **2014**, *6*, 2009–2026.
(12) Zhang, X.; Ai, Z. H.; Jia, F. L.; Zhang, L. Z. Generalized One-Pot Synthesis, Characterization, and Photocatalytic Activity of Hierarchical BiOX (X = Cl, Br, I) Nanoplate Microspheres. *J. Phys. Chem. C* **2008**, *112*, 747–753.
(13) Henle, J.; Simon, P.; Frenzel, A.; Scholz, S.; Kaskel, S. Nanosized BiOX (X = Cl, Br, I) Particles Synthesized in Reverse Microemulsions. *Chem. Mater.* **2007**, *19*, 366–373.
(14) Jiang, J.; Zhang, X.; Sun, P. B.; Zhang, L. Z. ZnO/BiOI Heterostructures: Photoinduced Charge Transfer Property and Enhanced Visible Light Photocatalytic Activity. *J. Phys. Chem. C* **2011**, *115*, 20555–20564.
(15) Huang, H. W.; He, Y.; Lin, Z. S.; Kang, L.; Zhang, Y. H. Two Novel Bi-Based Borate Photocatalysts: Crystal Structure, Electronic Structure, Photoelectrochemical Properties, and Photocatalytic Activity under Simulated Solar Light Irradiation. *J. Phys. Chem. C* **2013**, *117*, 22986–22994.
(16) Liu, Y. Y.; Son, W. J.; Lu, J. B.; Huang, B. B.; Dai, Y.; Whangbo, M. H. Composition Dependence of the Photocatalytic Activities of

DOI: 10.1021/am5065409
ACS Appl. Mater. Interfaces 2015, 7, 482–492

$BiOCl_{1-x}Br_x$ Solid Solutions under Visible Light. *Chem.—Eur. J.* **2011**, *17*, 9342−9349.
(17) Lin, H. L.; Li, X.; Cao, J.; Chen, S. F.; Chen, Y. Novel I^--Doped BiOBr Composites: Modulated Valence Bands and Largely Enhanced Visible Light Phtotocatalytic Activities. *Catal. Commun.* **2014**, *49*, 87−91.
(18) Gnayem, H.; Sasson, Y. Hierarchical Nanostructured 3D Flowerlike $BiOCl_xBr_{1-x}$ Semiconductors with Exceptional Visible Light Photocatalytic Activity. *ACS Catal.* **2013**, *3*, 186−191.
(19) Chang, X.; Yu, G.; Huang, J.; Li, Z.; Zhu, S.; Yu, P.; Cheng, C.; Deng, S.; Ji, G. Enhancement of Photocatalytic Activity over $NaBiO_3$/BiOCl Composite Prepared by an in Situ Formation Strategy. *Catal. Today.* **2010**, *153*, 193−199.
(20) Zhang, X.; Zhang, L. Z.; Xie, T. F.; Wang, D. J. Low-Temperature Synthesis and High Visible-Light-Induced Photocatalytic Activity of BiOI/TiO_2 Heterostructures. *J. Phys. Chem. C* **2009**, *133*, 7371−7378.
(21) Jiang, J.; Zhang, X.; Sun, P. B.; Zhang, L. Z. ZnO/BiOI Heterostructures: Photoinduced Charge-Transfer Property and Enhanced Visible-Light Photocatalytic Activity. *J. Phys. Chem. C* **2011**, *115*, 20555−20564.
(22) Cheng, H.; Huang, B.; Dai, Y.; Qin, X.; Zhang, X. One-Step Synthesis of the Nanostructured AgI/BiOI Composites with Highly Enhanced Visible-Light Photocatalytic Performances. *Langmuir* **2010**, *26*, 6618−6624.
(23) Shamaila, S.; Sajjad, A. K. L.; Chen, F.; Zhang, J. L. WO_3/BiOCl, A Novel Heterojunction as Visible Light Photocatalyst. *J. Colloid Interface Sci.* **2011**, *356*, 465−472.
(24) Zhang, J.; Xia, J. X.; Yin, S.; Li, H. M.; Xu, H.; He, M. Q.; Huang, L. Y.; Zhang, Q. Improvement of Visible Light Photocatalytic Activity over Flower-Like BiOCl/BiOBr Microspheres Synthesized by Reactable Ionic Liquids. *Colloids Surf.* **2013**, *A420*, 89−95.
(25) Xiao, X.; Hao, R.; Liang, M.; Zuo, X. X.; Nan, J. M.; Li, L. S.; Zhang, W. D. One-Pot Solvothermal Synthesis of Three-Dimensional (3D) BiOI/BiOCl Composites with Enhanced Visible-Light Photocatalytic Activities for the Degradation of Bisphenol-A. *J. Hazard. Mater.* **2012**, *233*, 122−130.
(26) Li, T. B.; Chen, G.; Zhou, C.; Shen, Z. Y.; Jin, R. C.; Sun, J. X. New Photocatalyst BiOCl/BiOI Composites with Highly Enhanced Visible Light Photocatalytic Performances. *Dalton Trans.* **2011**, *40*, 6751−6758.
(27) Cao, J.; Xu, B. Y.; Lin, H. L.; Luo, B. D.; Chen, S. F. Chemical Etching Preparation of BiOI/BiOBr Heterostructures with Enhanced Photocatalytic Properties for Organic Dye Removal. *Chem. Eng. J.* **2012**, *185*, 91−99.
(28) Cao, J.; Xu, B. Y.; Luo, B. D.; Lin, H. L.; Chen, S. F. Novel BiOI/BiOBr Heterojunction Photocatalysts with Enhanced Visible Light Photocatalytic Properties. *Cata. Comm.* **2011**, *13*, 63−68.
(29) Wang, J. L.; Yu, Y.; Zhang, L. Z. Highly Efficient Photocatalytic Removal of Sodium Pentachlorophenate with Bi_3O_4Br under Visible Light. *Appl. Catal. B* **2013**, *136*, 112−121.
(30) Tian, N.; Zhang, Y. H.; Huang, H. W.; He, Y.; Guo, Y. X. Influences of Gd Substitution on the Crystal Structure and Visible-Light-Driven Photocatalytic Performance of Bi_2WO_6. *J. Phys. Chem. C* **2014**, *118*, 15640−15648.
(31) Ye, L. Q.; Liu, J. Y.; Jiang, Z.; Peng, T. Y.; Zan, L. Facets Coupling of BiOBr-*g*-C_3N_4 Composite Photocatalyst for Enhanced Visible-Light-Driven Photocatalytic Activity. *Appl. Catal. B* **2013**, *142*, 1−7.
(32) Huang, H. W.; He, Y.; He, R.; Lin, Z. S.; Zhang, Y. H.; Wang, S. C. $Y(IO_3)_3$ as a Novel Photocatalyst: Synthesis, Characterization, and Highly Efficient Photocatalytic Activity. *Inorg. Chem.* **2014**, *53*, 8114−8119.
(33) Wang, X. F.; Li, S. F.; Ma, Y. Q.; Yu, H. G.; Yu, J. G. H_2WO_4·H_2O/Ag/AgCl Composite Nanoplates: A Plasmonic Z-Scheme Visible-Light Photocatalyst. *J. Phys. Chem. C* **2011**, *115*, 14648−14655.
(34) Perdew, J. P.; Burke, K.; Ernzerhof, M. Generalized Gradient Approximation Made Simple. *Phys. Rev. Lett.* **1996**, *77*, 3865−3868.
(35) Segall, M. D.; Lindan, P. L. D.; Probert, M. J.; Pickard, C. J.; Hasnip, P. J.; Clark, S. J.; Payne, M. C. First-Principles Simulation: Ideas, Illustrations and the CASTEP Code. *J. Phys.: Condens. Matter.* **2002**, *14*, 2717−2744.
(36) Ohko, Y.; Hashimoto, K.; Fujishima, A. Kinetics of Photocatalytic Reactions under Extremely Low-Intensity UV Illumination on Titanium Dioxide Thin Films. *J. Phys. Chem. A* **1997**, *101*, 8057−8062.
(37) Huang, H. W.; Yao, J. Y.; Lin, Z. S.; Wang, X. Y.; He, R.; Yao, W. J.; Zhai, N. X.; Chen, C. T. $NaSr_3Be_3B_3O_9F_4$: A Promising Deep-Ultraviolet Nonlinear Optical Material Resulting from the Cooperative Alignment of the $[Be_3B_3O_{12}F]^{10-}$ Anionic Group. *Angew. Chem., Int. Ed.* **2011**, *50*, 9141−9144.
(38) Wu, F.; Liu, Y. F.; Yu, G. X.; Shen, D. F.; Wang, Y. L.; Kan, E. J. Visible-Light-Absorption in Graphitic C_3N_4 Bilayer: Enhanced by Interlayer Coupling. *J. Phys. Chem. Lett.* **2012**, *3*, 3330−3334.
(39) Kim, H.; Borse, P.; Choi, W.; Lee, J. Photocatalytic Nanodiodes for Visible-Light Photocatalysis. *Angew. Chem., Int. Ed.* **2005**, *44*, 4585−4589.
(40) Hosseini, Z.; Taghavinia, N.; Sharifi, N.; Chavoshi, M.; Rahman, M. Fabrication of High Conductivity TiO_2/Ag Fibrous Electrode by the Electrophoretic Deposition Method. *J. Phys. Chem. C* **2008**, *112*, 18686−18689.
(41) Huang, H. W.; Liu, K.; Chen, K.; Zhang, Y. L.; Zhang, Y. H.; Wang, S. C. Ce and F Comodification on the Crystal Structure and Enhanced Photocatalytic Activity of Bi_2WO_6 Photocatalyst under Visible Light Irradiation. *J. Phys. Chem. C* **2014**, *118*, 14379−14387.
(42) Chen, S. F.; Hu, Y. F.; Meng, S. G.; Fu, X. L. Study on the Separation Mechanisms of Photogenerated Electrons and Holes for Composite Photocatalysts g-C_3N_4-WO_3. *Appl. Catal. B: Environ.* **2014**, *150*, 564−573.
(43) Kubacka, A.; Fernández-García, M.; Colón, G. Photocatalysis on Advanced Nanoarchitectures for Solar Photocatalytic Applications. *Chem. Rev.* **2012**, *112*, 1555−1614.

DOI: 10.1021/am5065409
ACS Appl. Mater. Interfaces 2015, 7, 482−492